RESEARCH PAPER

Development of a Novel CuWO₄/SnO₂ Heterogenous Photocatalyst for Effective Rose Bengal Dye Degradation under Visible Light

Eswaran Kamaraj[1], Kavitha Balasubramani[2,*]

* kaviravee@gmail.com

[1] School of Chemical Engineering, Yeungnam University, Gyeongsan 38541, Repubic of Korea
[2] Post Graduate and Research Department of Chemistry, Cardamom Planters' Association College, Bodinayakanur-625513, Tamilnadu, India

Abstract: A heterostructure photocatalyst composed of CuWO₄-modified SnO₂ (CuWO₄/SnO₂) was synthesized using a simple wet-chemical methods and evaluated for its ability to degrade Rose Bengal (RB) dye under visible light irradiation. Comprehensive characterization of the samples was conducted using Ultraviolet-visible diffuse reflectance spectroscopy (UV-vis-DRS), X-ray diffraction (XRD), scanning electron microscopy (SEM) with energy-dispersive X-ray spectroscopy (EDS), transmission electron microscopy (TEM), high-resolution TEM (HR-TEM), Brunauer-Emmett-Teller surface analysis (BET), and X-ray photoelectron spectroscopy (XPS). The results demonstrated that CuWO₄/SnO₂ exhibited significantly superior photocatalytic activity compared to CuWO₄ or SnO₂ alone. This enhanced efficiency is attributed to the effective charge transfer between SnO₂ and CuWO₄ nanoparticles, which considerably reduces electron-hole recombination energy levels. Optimal conditions for maximum RB degradation under visible light were found to be a pH of 8, a dye concentration of 20 μM, and a photocatalyst dosage of 0.2 g/L, achieving a high degradation efficiency of 98.5% within 180 minutes. The outstanding photocatalytic performance of CuWO₄/SnO₂ is primarily due to the profecient separation of light induced electron-hole pairs. The reactive species involved in the photocatalytic degradation of RB include holes (h⁺) and superoxide radicals (O2˙⁻). This study highlights the potential of CuWO₄/SnO₂ as an effective photocatalyst for environmental remediation applications.

Keywords: Surface modification, CuWO₄/SnO₂, Photodegradation, Rose bengal.

1. INTRODUCTION

Natural contamination because of the transfer of dangerous and cancer-causing natural dye is a standout amongst the most imperative issues on the planet today. Out of different classes of dye, xanthene dye are most generally utilized. Xanthene dye are class of dye, described by nearness of xanthene core with sweet-smelling bunches as a chromophore. These dye are widely utilized as a colorant in material, printing and coloring ventures. Be that as it may, these colors are accounted for to be genotoxic, mutagenic, cytotoxic and cytostatic [1– 5]. RB is an essential xanthene color and is generally utilized as a part of eye drops, coloring, printing and bug spray. The utilization of semiconductor photocatalysis in the corruption of natural colors has pulled in serious consideration amid the previous two decades [6].

Metal oxide photocatalysts have gained substantial attention for their role in environmental remediation, with TiO₂ and SnO₂ being particularly prominent examples. Both

SnO₂ and TiO₂ are isostructural polymorphs sharing the same crystal symmetry, crystallizing in the rutile structure (space group no. 136; D14 4h; P42/mnm). Additionally, TiO₂ can also exist in the anatase phase (space group no. 141; D19 4h; I41/amd). The differences in their Born effective charges are due to the distinct nature of Ti-O and Sn-O bonding, which can be explained using the bond charge model [7]. Despite their similarities in crystal structure, bond lengths (1.90 Å), chemical bonds, and electronic band-gap energies (Eg 3–4 eV), SnO₂ and TiO₂ exhibit unique optical and electronic properties. SnO₂ is generally optically transparent with high electron conductivity, while TiO₂ is known for its strong optical absorption properties and lower electron mobility, which is attributed to electron and hole trapping mechanisms [8].

SnO₂ is a nontoxic, economically viable semiconductor oxide known for its stable physicochemical properties and photocorrosion resistance [9, 10]. However, its wide 3.6 eV bandgap limits light absorption to the UV region (λ< 400 nm), just 4% of the solar spectrum [11].

Its photocatalytic efficiency is further hindered by rapid electron-hole recombination, low adsorption capacity, and poor reusability [12, 13].To harness sunlight more effectively in the visible region, it is essential to enhance photocatalysts that operate under visible light. Enhancing electron-hole separation can be attained *via* creating junctions and chemical potential gradients within photocatalysts. Various strategies to improve photocatalytic performance include coating with noble metal nanoparticles [14–16], doping with nonmetal and transition metal ions [17–18], and forming semiconductor composites. These approaches aim to extend light absorption, reduce recombination rates, and increase the overall efficiency and reusability of the photocatalysts [19, 20].

Combining two semiconductor nanoparticles with different band gaps has confirmed to be an successful way for reducing electron-hole recombination, as demonstrated in numerous studies [21, 22]. Recently, metal tungstate nanoparticles have fascinated significant consideration due to their narrow band gaps, which construct them outstanding photosensitizers for enhancing the photocatalytic activity of metal oxides [23, 24]. $CuWO_4$, a particularly promising candidate, belongs to the Aurivillius family of layered perovskites. This *n*-type material is capable of absorbing visible light, making it an ideal component for improving photocatalytic performance [25, 26].

To the extent of our knowledge, the photodegradation of RB dye using $CuWO_4/SnO_2$ has been barely explored. This study aims to evaluate the photocatalytic activity of $CuWO_4/SnO_2$ for RB degradation under visible light. We investigated the impact of various operational parameters, including pH, dye concentration, and catalyst dosage, on the photocatalytic degradation efficiency. Furthermore, we proposed and analyzed a plausible mechanism for the photodegradation of RB using $CuWO_4/SnO_2$.

2. EXPERIMENTAL PROCEDURES

2.1. Materials

Stannous chloride ($SnCl_4.5H_2O$), copper sulfate ($CuSO_4.5H_2O$), sodium tungstate ($Na_2WO_4.2H_2O$), sodium hydroxide (NaOH), and methanol (MeOH) were sourced from Merck

Chemicals (Mumbai, India), whereas the synthetic dye RB was acquired from Sigma Aldrich. All the reagents and chemicals were of analytical grade and employed without additional purification. Double-distilled water was served as solvent in all photodegradation experiments.

2.2. Synthesis

2.2.1. Synthesis of SnO_2

The process of synthesizing SnO_2 nanoparticles commenced with a precipitation technique. Initially, 6 g of $SnCl_4 \cdot 5H_2O$ were dissolved in 100 ml of double-distilled water. A calculated quantity of aqueous ammonia solution was gradually introduced into the stannous chloride solution until the pH reached 7, all while vigorously stirring for a duration of 2 h. The resulting white precipitates were then gathered through centrifugation, followed by several rinses with double-distilled water and absolute ethanol. Subsequently, the gathered precipitates underwent drying at 120°C for 2 h. Finally, the dried solid underwent sintering in air at 500°C for 2 h.

2.2.2. Synthesis of $CuWO_4$

$CuWO_4$ was synthesized using a precipitation method. Initially, 5 g of $CuSO_4 \cdot 5H_2O$ (20.27 mmol) and 6.7 g of $Na_2WO_4 \cdot 2H_2O$ (20.27 mmol) were dissolved separately in water. The solutions are then combined, and the pH is adjusted to 8 using NaOH (0.1 M) to initiate nanoparticle precipitation. The resulting solid was filtered, washed with water to remove impurities, and the the $CuWO_4$ precipitate was driet at 120°C. subsequently, dried nanoparticles underwent calcination at 500°C for 4 h.

2.2.3. Synthesis of $CuWO_4/SnO_2$

$CuWO_4/SnO_2$ nanocomposites were synthesized *via* chemical impregnation technique. Intially, 1.99 g of $CuWO_4$ and 5 g of SnO_2 was dispersed in 100 ml of ethanol. Subsequently, the entire mixture was refluxed at 70°C for 2 h. The resulting solid was filtered, dried at 90°C for 6 h and then calcined at 500°C for 2 h.

2.3. Characterization

To analyze the synthesized products, a range of analytical techniques were utilized. UV-vis-DRS data was collected using a JASCO V-550 double beam spectrophotometer with $BaSO_4$ as a reference. XRD analysis employed an XPERT PRO X-RAY diffractometer operating at 25°C

with Cu Kα radiation. SEM imaging was conducted with a JEOL JSM 6701F instrument, accompanied by EDS for elemental analysis. TEM images were captured using a TEM TECNAI G2 model, while HR-TEM analysis utilized a JOEL JEM-2010 instrument. XPS measurements were carried out using a VG ESCALAB 210 XPS spectrometer system with a Mg Kα source. BET nitrogen adsorption-desorption isotherm analysis was performed with a Micromeritics ASAP 2020 apparatus. Absorption spectra were recorded using a JASCO-V-530 UV-visible spectrophotometer. Photocatalytic experiments took place in an immersion type photoreactor (HIPR-Compact-P-8/125/250/400), with pH monitored using a EUTECH instrument pH meter.

2.4. Measurement of Photocatalytic Activity

The efficiency of the synthesized compounds in photocatalysis was estimated by measuring the degradation of a dye pollutant under visible light exposure. Photocatalytic tests were carried out using an immersion-type photoreactor [27], where a 300 W mercury lamp was housed in a cylindrical chamber surrounded by a circulating water jacket for temperature control. Each experiment utilized 0.2 grams of the photocatalyst suspended in a 300 mL aqueous solution containing 20 μM RB dye. Prior to exposure to light, the solution was stirred in darkness for 30 minutes to reach an adsorption-desorption equilibrium. At specified intervals, the concentration of RB dye was determined spectrophotometrically at 545 nm. The extent of RB photodegradation was then calculated using Equation 1.

$$Photodegradation\,(\%) = \frac{C_0 - C}{C_0} \times 100 \qquad (1)$$

Where C_0 represent the inital concentration of RB dye prior to light, while C is denotes concentration of RB dye following a specific period of irradiation. This equation quantifies the percentage of photodegradation of RB dye over the course of the experiment.

3. RESULTS AND DISCUSSION

3.1. UV-vis-DRS Analysis

Fig. 1(a) presents the UV-vis-DRS spectra for SnO_2, $CuWO_4$, and the $CuWO_4/SnO_2$ composite. The absorption edge of the $CuWO_4/SnO_2$ composite shows a significant red shift in comparison to the individual SnO_2 and $CuWO_4$ samples. This shift is attributed to the incorporation of $CuWO_4$ into SnO_2. To calculate the band gap, the Tauc relationship [28] was employed.

$$A(h\nu) = A(h\nu - E_g)^{\frac{1}{2}} \qquad (2)$$

where the absorption coefficient α is obtained from the scattering and reflectance spectra based on the Kubelka–Munk theory, $h\nu$ represents the photon energy, and A is the absorption constant for direct transition. The plot of $(\alpha h\nu)^2$ versus photon energy ($h\nu$) is depicted in Fig. 1(b). The calculated band gap energy (E_g) values are 3.10 eV, 2.04 eV, and 1.34 eV for SnO_2, $CuWO_4$, and $CuWO_4/SnO_2$, respectively.
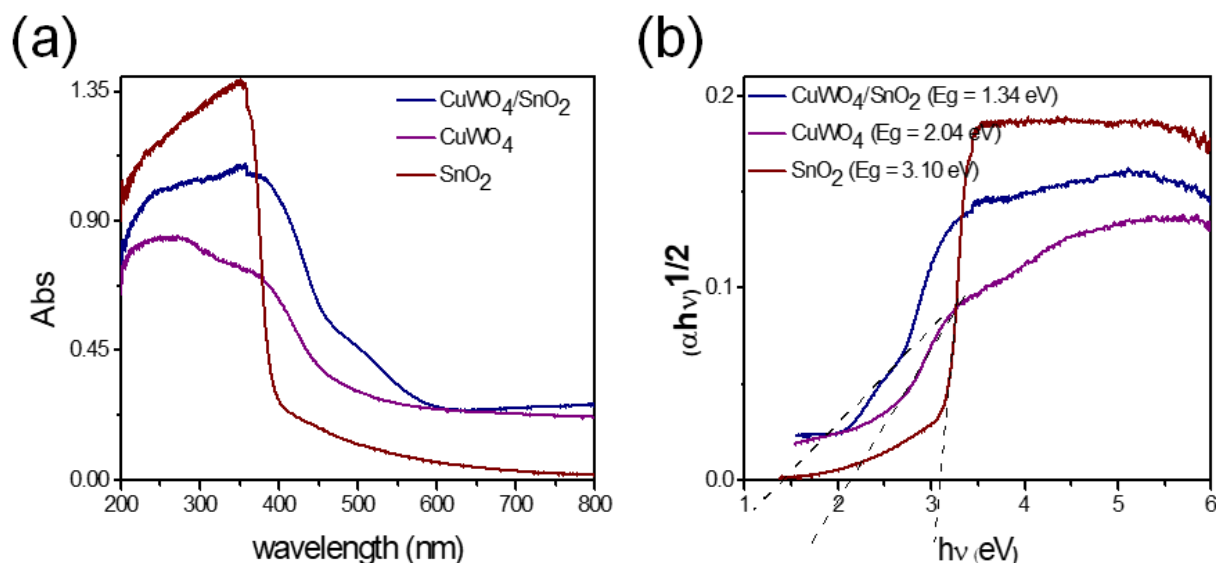

Fig. 1. (a) UV-vis-DRS spectra of SnO_2, $CuWO_4$, $CuWO_4/SnO_2$ and (b) Tauc of SnO_2, $CuWO_4$, $CuWO_4/SnO_2$.

Notably, the band gap energy of $CuWO_4/SnO_2$ is lower than that of SnO_2 and $CuWO_4$, indicating a significant alteration in the electronic structure of SnO_2 due to electron transfer from $CuWO_4/SnO_2$. Consequently, the coupled nanoparticles facilitate relatively efficient electron-hole separation.

3.2. XRD Analysis

The XRD of $CuWO_4/SnO_2$, $CuWO_4$, and SnO_2 nanoparticles were shown in Fig. 2. The standard XRD pattern reveals characteristic peaks at 26.49°, 33.77°, 51.68°, 54.71°, and 65.89° corresponding to the crystal planes of SnO_2 at 110, 101, 200, 211 and 220, respectivley (JCPDS Card No. 88-0287).
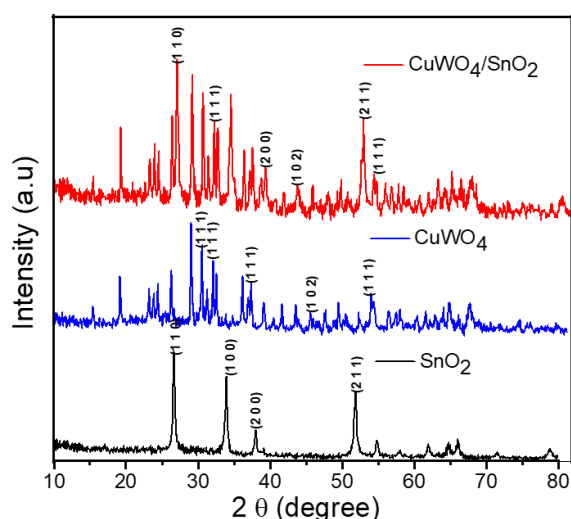

Fig. 2. XRD pattern of SnO_2, $CuWO_4$ ande $CuWO_4/SnO_2$

The XRD analysis of SnO_2 confirms its tetragonal primitive crystalline phase, with lattice parameters a= 4.737 nm, c= 3.186 nm. For $CuWO_4$, a series of distintive peaks at 19.0° (100), 24.0° (110), 25.9° (101), 28.7° (111), 30.1° (111), 31.6° (111), 32.1° (111), 35.6° (012), 36.8° (002), 39.8° (120) and 42.9° (102) are observed, corresponding to the scheelite primitive phase with P1 space group symmetry (PCPDF Card No. 88-0269). The solid intensity and narrow width of the $CuWO_4$ diffraction peaks indicate high crystallinity. The XRD of $CuWO_4/SnO_2$ reveals the consolidated diffraction pattern, displays the orthorhombic primitive phases of SnO_2 and anthronic crystalline phases of $CuWO_4$. The average crystallite size of the sample was determined using the Scherrer equation (Eq. 3) [29]:

$$D = \frac{K\lambda}{\beta cos\theta} \tag{3}$$

where β represents the full width half maximum of diffraction peak, θ is the diffraction angle, and K= 0.89 is a coefficient. λ is X-ray wavelength corresponding to the Cu Kα radiation. The calculated average crystallite size of SnO_2, $CuWO_4$, and $CuWO_4/SnO_2$ was 33.46 nm, 40.6 nm, and 30.9 nm respectively. It is worth noting slight reduce in the crystallite size of SnO_2 following surface modification with $CuWO_4$.

3.3. SEM and EDS Analysis

The surface morphologies of SnO_2, $CuWO_4$, and $CuWO_4/SnO_2$ were characterized by SEM and presented in Fig. 3(a), 3(b) and 3(c) respectively. The elemental composisiton of the samples, including Sn, W, Cu, and O was confirmed by EDS analysis, and the results are depicted in Fig. 3(d). In the EDS spectra, distinct peaks corresponding to Sn, Cu, W, and O are unambiguously noted at their characteristic energies. From SEM images, it can be observed SnO_2 and $CuWO_4$ nanoparticles exhibited spherical-like structures. However, $CuWO_4/SnO_2$ displays sponge-like morphology with small spherical structure. The catalyst $CuWO_4/SnO_2$ appears to be even smaller size but more aggregated, which can be recognized to the high surface energy associated with the smaller-sized particles.

3.4. TEM and HR-TEM Analysis

Fig. 4(a) shows the TEM morphology of $CuWO_4/SnO_2$ nanoparticles. The micrographs of the photocatalyst demonstrate that the $CuWO_4$ particles are well dispersed on the SnO_2 surface. The size of the SnO_2 nanoparticles assessed from the TEM picture is around 31.2 nm (Table 1), which is in great concurrence with XRD result. The crystalline nature, distribution, and existence of $CuWO_4$ in SnO_2 were additionally examined utilizing HR-TEM examination and the outcomes appear in Fig. 4(b).

It is clearly seen that $CuWO_4/SnO_2$ is relatively uniform, dispersive and sponges with small spheres like structure. The outcomes reveal that the unique nanosphere assembly structure would allow higher exposure efficiency of the active site to the photocatalyst, and hence is relied upon to be ideal for improved photocatalytic movement for the removal of dye molecules. Additionally demonstrating polycrystalline nature of the photocatalyst. The selected-area electron

4

diffraction (SAED) pattern appears (Fig 4(c)) showed polycrystalline rings and number of continuous random bright spots revealed that the diffraction rings could be indexed as (110), (111), (102), (211), and (111) planes. These outcomes are great concurrence with the watched XRD examination.
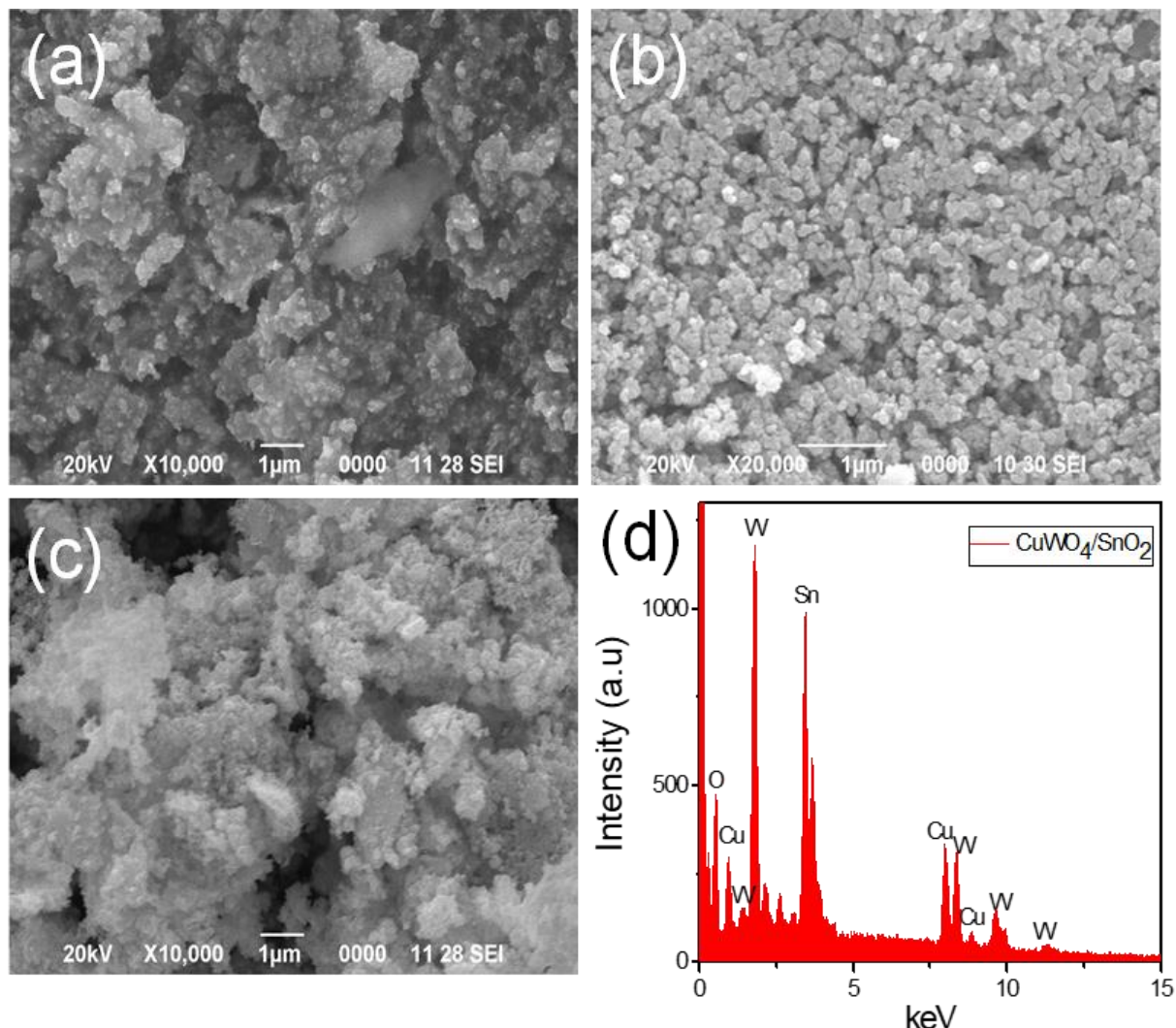

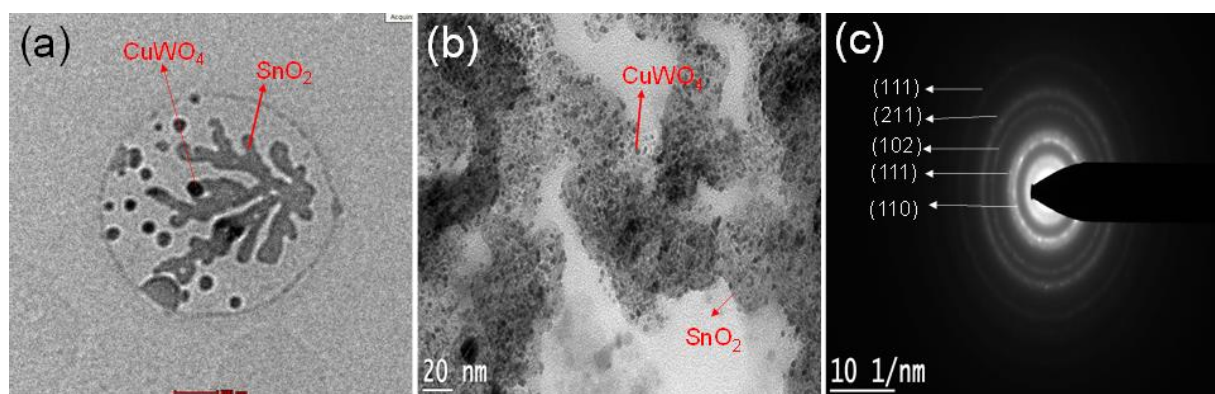**Fig. 3.** SEM images showing (a) SnO$_2$, (b) CuWO$_4$, (c) CuWO$_4$/SnO$_2$ and (d) the EDX spectrum of CuWO$_4$/SnO$_2$.

Fig. 4. (a) TEM micrographs (b) HR-TEM (c) SAED pattern of CuWO$_4$/SnO$_2$.

5

Kavitha Balasubramani et al.

3.5. BET (Brunauer–Emmett–Teller) Analysis

Fig. 5(a-c) gives the nitrogen adsorption-desorption isotherms and pore diagram for SnO_2, $CuWO_4$, and $CuWO_4/SnO_2$ nanocomposites. The $CuWO_4/SnO_2$ exhibits Type IV isotherm (hysteresis loop) in view of Brunauer-Deming-Deming-Teller (BDDT) classification, representing the presence of mesoporous. The BET surface region of $CuWO_4/SnO_2$ (123.92 m²/g) was observed to be higher than $CuWO_4$ (112.99 m²/g) and SnO_2 (35.73 m²/g). The BJH size distribution evidenced an average pore volume of about 0.29 cm³/g for $CuWO_4/SnO_2$, which is higher than another two bare nanoparticles. The outcome reveals that surface modifications are effectively accomplished in two metal oxides. The high surface area and mesoporous nature of $CuWO_4/SnO_2$ spongy microspheres provide numerous adsorption sites for dye degradation, enhancing photocatalytic performance due to their higher BET specific surface area.
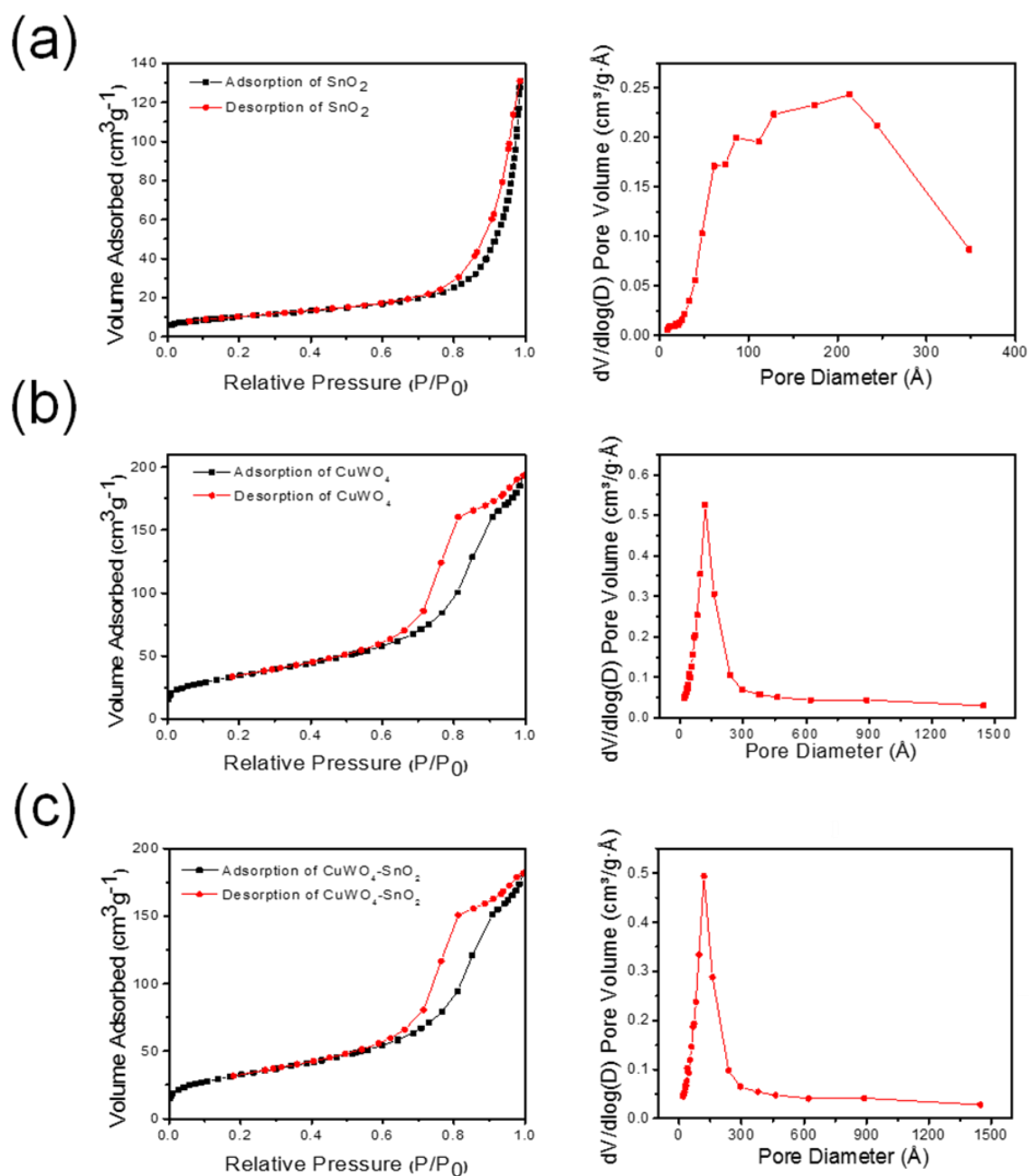

Fig. 5. Nitrogen adsorption-desorption isotherms and pore size distribution of (a) SnO_2 (b) $CuWO_4$ and (c) $CuWO_4/SnO_2$

3.6. XPS Analysis

The elemental composition of the prepared $CuWO_4/SnO_2$ was characterized by the XPS technique. Fig. 6(a), 6(b), 6(c) and 6(d) displays XPS spectra of the Sn, Cu, W and O As displayed in Fig. 6(a), the binding energy peaks at 487 eV and 496 eV are recognized to Sn^{4+} $3d_{5/2}$ and Sn^{4+} $3d_{3/2}$ respectively [30]. The Cu (2p) region exhibits Cu ($2p_{3/2}$) and Cu ($2p_{1/2}$) peaks at 935 eV and 959 eV, respectively. Additionally, weak satellite peaks at 973 eV indicate a minimal presence of CuO, likely resulting from the oxidation of Cu^{2+} species on the composite surface at room temperature [31] (Fig. 6(b)). In Fig. 6(c), peaks at approximately 3.5 eV for $W4f_{7/2}$ and 3.7 eV for $W4f_{5/2}$ suggest that W is present in the $CuWO_4$ samples as W^{+6} [32]. The O1s peak, observed with a binding energy of 531.27 eV (Fig. 6(d)), aligns with the O1s of O^{2-} [33, 34]. From this analysis, it can be concluded that the $CuWO_4/SnO_2$ nanocomposites comprise Sn^{4+}, Cu^{2+}, W^{6+}, and O^{2-}, consistent with the XRD results.

3.7. Photocatalytic Activity

3.7.1. *Photocatalytic degradation of RB*

Photocatalytic investigates were conducted with an initial RB concentration of 20 µM, a catalyst concentration of 0.2 g/L, at pH 8, and an irradiation duration of 180 minutes. Fig. 7(a) illustrates the UV-vis spectra of RB at different irradiation times (0 min, 30 min, 60 min, 90 min, 120 min, 150 min, and 180 min) using the $CuWO_4/SnO_2$ catalyst. The prominent peak at λ_{max}= 545 nm progressively diminishes as irradiation time increases, indicating RB degradation on the $CuWO_4/SnO_2$ surface. Figure 7(b) shows the photodegradation curves of RB with the prepared catalyst. Control tests conducted without a catalyst demonstrated minimal RB degradation, underscoring the role of photocatalysis.
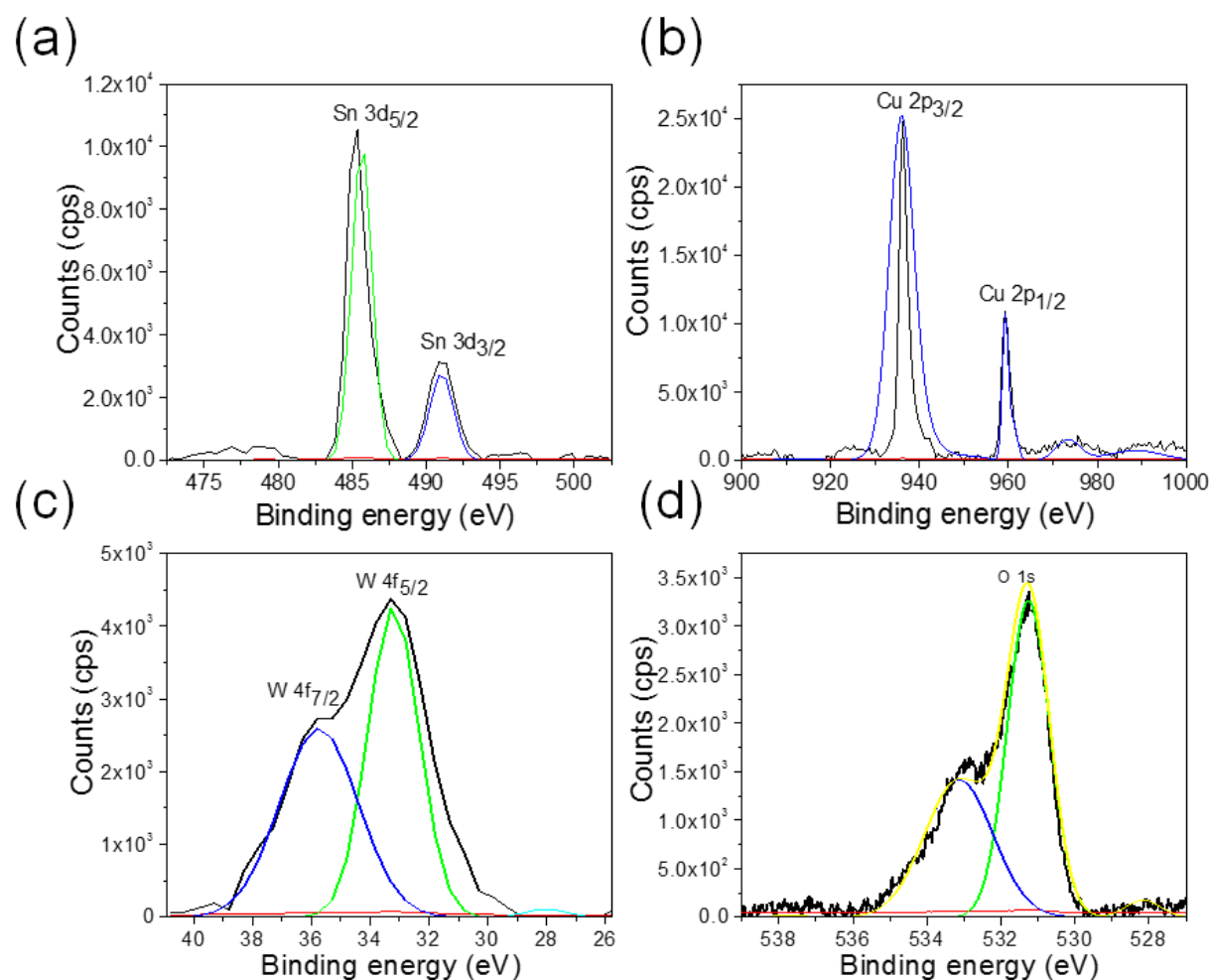

Fig. 6. XPS spectra of $SnO_2/CuWO_4$ photocatalysts: (a) Sn 3d, (b) Cu 2p, (c) W 4f, and (d) O1s

The photodegradation efficiency of $SnO_2/CuWO_4$ (92%) is significantly higher compared to SnO_2 (75%) and $CuWO_4$ (52%), as depicted in Fig. 7(d). This suggests that modifying SnO_2 with $CuWO_4$ greatly enhances its photodegradation efficiency by improving electron-hole separation on the photocatalytic surface. The degradation of RB with the prepared photocatalyst follows a pseudo-first-order kinetic model, described by the following equation:

$$-\ln\left(\frac{c}{c_0}\right) = k_t \qquad (4)$$

In the provided equation, C_0 denotes the initial concentration of RB at t= 0 minutes, C represents the concentration of RB at irradiation time 't', and K is the rate constant. Fig. 7(c) illustrates the plot of $-\ln(C/C_0)$ versus irradiation time 't', which demonstrates a linear relationship. The first-order rate constants are derived from the slopes of the $-\ln(C/C_0)$ versus 't' plots. The calculated rate constants are 1.176×10^{-2} s^{-1} for $CuWO_4/SnO_2$, 1.077×10^{-3} s^{-1} for $CuWO_4$, and 8.3×10^{-3} s^{-1} for SnO_2.

Building on prior research [35-37], we propose a mechanism explaining the enhanced photocatalytic activity of $CuWO_4/SnO_2$. Fig. 8(a) depicts a schematic illustrating the electron transfer process between $CuWO_4$ and SnO_2 under visible light.
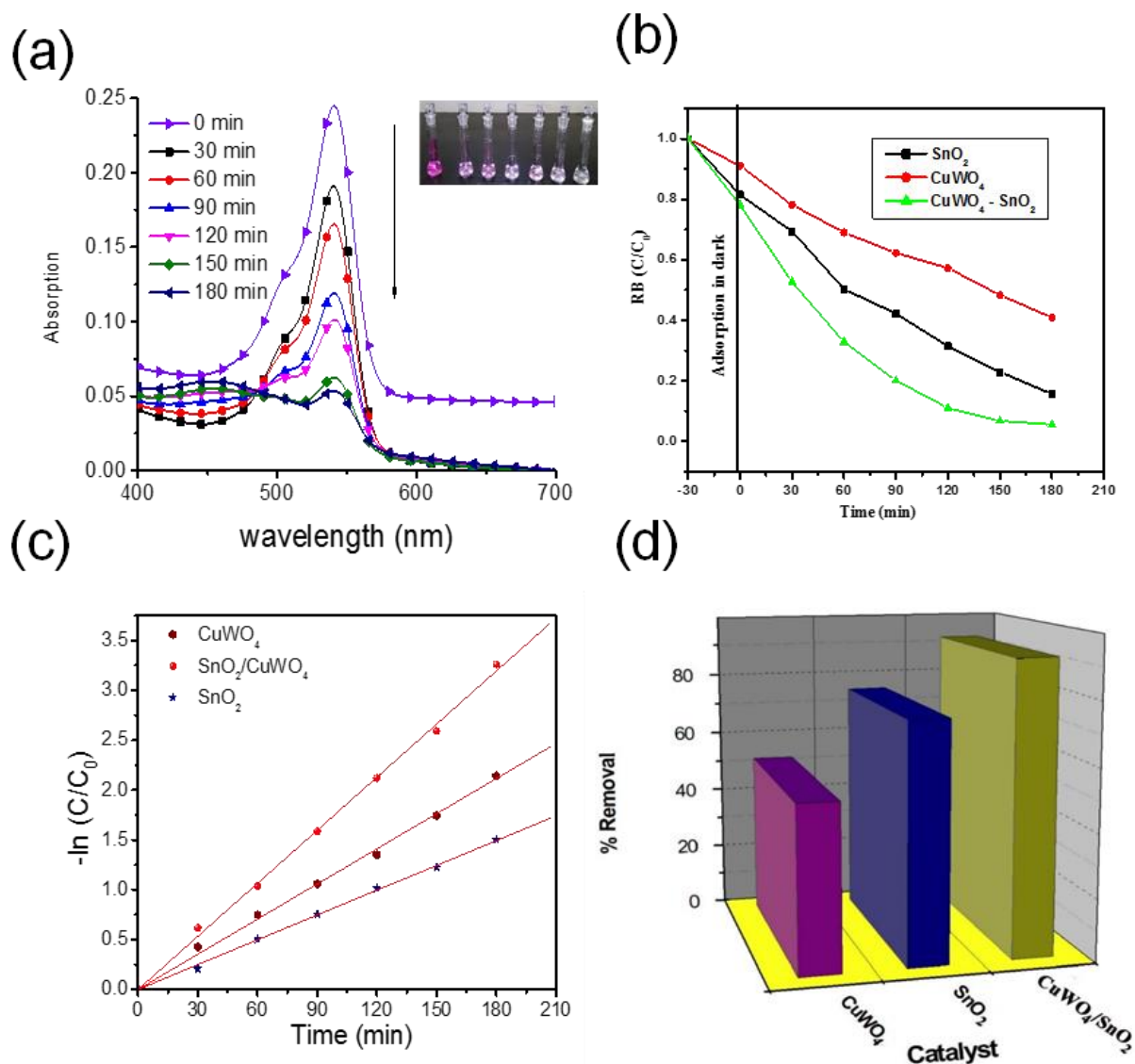

Fig. 7. (a) the dynamic alterations in the UV-Vis spectra of RB when subjected to visible light in the presence of $CuWO_4/SnO_2$. (b) the photocatalytic degradation process of RB with SnO_2, $CuWO_4$, $CuWO_4/SnO_2$. (c) a comparative analysis of the photocatalytic degradation percentages of RB with SnO_2, $CuWO_4$, $CuWO_4/SnO_2$. (d) the kinetic plot of $-\ln(C/C_0)$ against irradiation time for RB photodegradation.
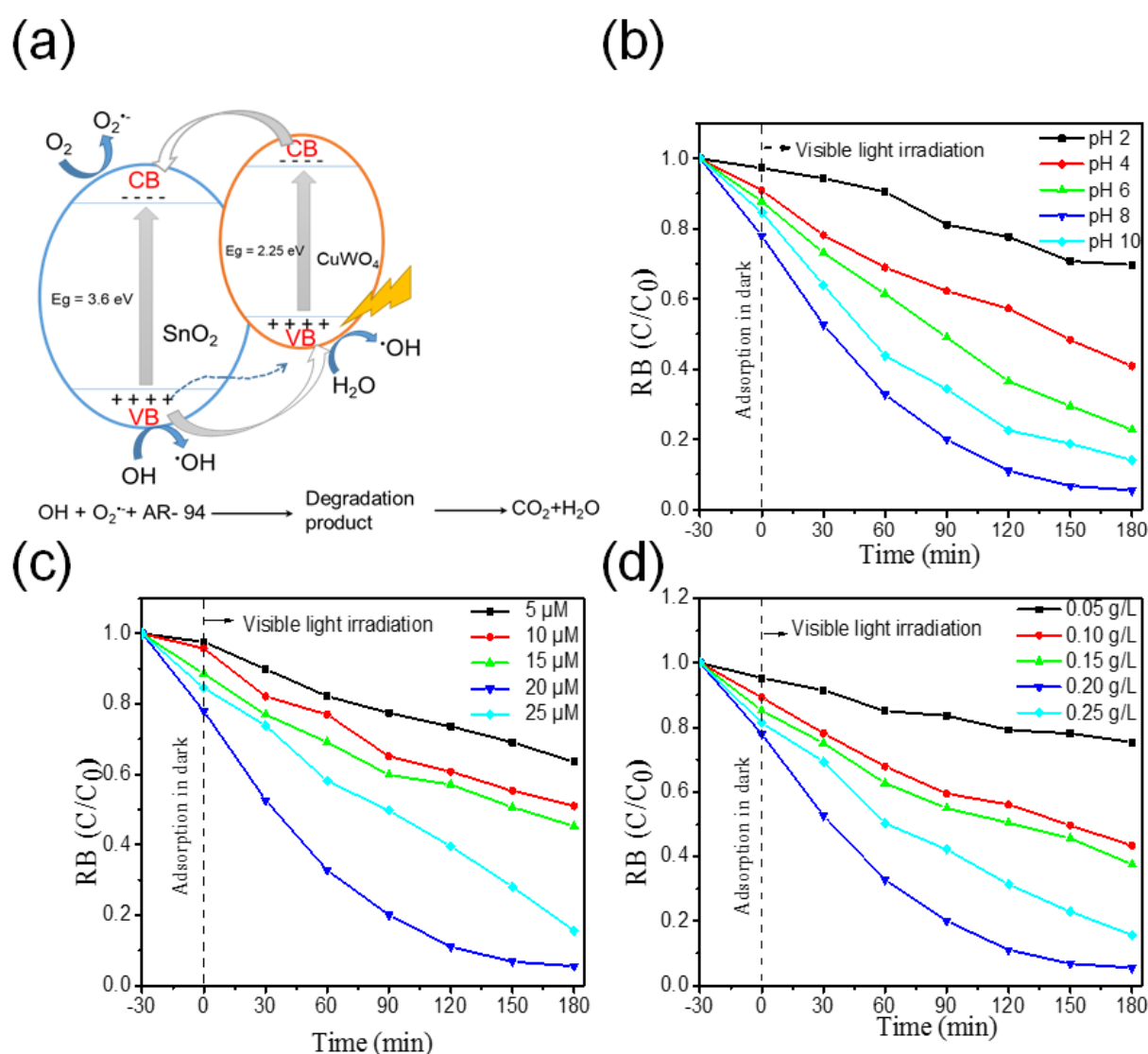
Fig. 8. (a) Schematic diagram showing the feasible photodegradation mechanism of CuWO₄/SnO₂ towards RB degradation, (b) Effect of pH on the photodegradation of RB, (c) Effect of RB concentration on photodegradation using CuWO₄/SnO₂ and (d) effect of catalytic concentration on the photodegradation of RB.

Upon light exposure, $CuWO_4$ absorbs photons with energies matching its band gap, generating electron-hole pairs in its conduction band (CB) and valence band (VB). Following photoexcitation, the electrons move to the CB while positive holes remain in the VB. The electrons in $CuWO_4$ can easily migrate to the CB of SnO_2 [38], while the positive holes move in the converse direction. The holes can react with H_2O to yield hydroxyl radicals (•OH), and the electrons can react with dissolved oxygen to form superoxide radicals (O_2•-). The holes high redox potential than the •OH/OH⁻ and •OH/H_2O pairs, while the electrons have a lower redox potential compared to the O_2/O_2•- pair. These highly reactive free radicals interact with dye molecules on photocatalyst's surface, leading to the RB's degradation [39].

3.7.2. Effect of pH

Photodegradation efficiency is significantly influenced by the adsorption of RB on the surface of the catalyst, which in turn depends on the solution's pH. To explore this, the result of pH on photocatalytic degradation was studied at various pH levels, with the results presented in Fig. 8(b). The degradation of RB increased as the pH was raised from 2 to 8, reaching an optimum at pH 8. However, further rising the pH to 10 resulted in a diminish in degradation efficiency. The optimal pH for effective RB removal is pH 8, as shown in

Fig. 8(b). It is widely understood that photocatalytic reactions begin with the photogeneration of electron-hole pairs [40]. The primary oxidative species in the photodegradation process are photogenerated •OH radicals, which attack the dye molecule's chromophores. When the pH exceeds 8, the rate of photocatalytic degradation decreases. This can be indorsed to the amplified generation of $O_2^{•-}$ radicals, produced by the abstraction of electrons by dissolved oxygen, which are responsible for reducing dye molecules. Beyond pH 8, the excess $O_2^{•-}$ radicals render the semiconductor surface negatively charged, hindering the dye molecules' approach to the semiconductor surface. This negatively charged surface restricts the interaction between the dye and the catalyst, resulting in a diminished rate of RB photodegradation [41].

3.7.3. Effect of initial RB concentration

The impact of initial RB dye concentration (5 – 25 μM) on photocatalytic degradation was studied at pH 8 with a $CuWO_4/SnO_2$ dosage of 0.2 g/L, as shown in Fig. 8(c). The data indicate a decrease in the photodegradation percentage of RB as the initial RB concentration increases. This trend is due to a higher number of dye molecules adhering to the photocatalyst's surface at elevated dye concentrations, while the amount of reactive species remains constant. As per Beer-Lambert's law, higher dye concentrations reduce the effective path length of photons incoming the reaction mixture, decreasing the production of reactive oxygen species and thus lowering photodegradation efficiency [42].

3.7.4. Effect of catalyst loading

To optimize the dosage of the photocatalyst for RB degradation, experiments were conducted with varying amounts of $CuWO_4/SnO_2$ ranging from 0.05 g/L to 0.25 g/L. Throughout the experiments, the RB concentration was maintained at 20 μM and pH at 8. The finding, as depicted in Fig. 8(d), indicate that photodegradation efficiency increased as the catalyst dosage rose from 0.05 to 0.2 g/L. However, further increments in dosage resulted in a decline in efficiency. The optimal loading of the catalyst was determined to be 0.2 g/L. The enhancement in removal efficiency up to 0.2 g/L can be attributed to increased dye molecule adsorption on the catalyst surface and the larger illuminated surface area. Nevertheless, beyond 0.2 g/L, additional $CuWO_4/SnO_2$ did not significantly improve degradation. This is likely due to particle aggregation, reducing the available interfacial surface area. Excessive catalyst amounts can impede light penetration due to this aggregation, blocking light and reducing active sites on the catalyst surface, consequently diminishing degradation efficiency. It's noteworthy that in the absence of the photocatalyst, no significant degradation of RB was observed, suggesting the dye's resistance to self-photolysis in aqueous solution under visible light [43].

4. CONCLUSIONS

The $CuWO_4/SnO_2$ visible light photocatalyst was successfully designed and synthesized using a simple chemical impregnation method. Compared to bare SnO_2 and $CuWO_4$, the $CuWO_4$-modified SnO_2 exhibited superior photocatalytic properties and significantly enhanced degradation performance for RB dye. The photocatalytic studies highlight the importance of optimizing degradation parameters such as pH (8), dye concentration (20 μM), and catalyst dosage (0.2 g/L) to achieve a high degradation rate (1.176×10^{-2} s^{-1}). These optimized conditions are crucial for the practical application of photocatalytic processes. This integration process enhances the efficiency of photocatalysis, as the simultaneous application of photocatalysis and visible light irradiation promotes a synergistic degradation effect rather than a merely additive one. This approach demonstrates a promising strategy for improving the effectiveness of advanced oxidation processes in environmental remediation.

ACKNOWLEDGMENT

REFERENCES

[1]   Chequer, F.M.D., Venâncio, V. de P., Bianchi, M. de L.P. and Antunes, L.M.G., "Genotoxic and Mutagexic effects of

erythrosine B, a xanthan food dye, on HepG2 cells." Food Chem. Toxicol., 2012, 50, 3447-3451.

[2] Walthall, W.K. and Stark, J.D., "The acute and chronic toxicity of two xanthene dyes, fluorescein sodium salt and Phloxine B to Daphnia pulex." Environ. Pollut., 1999, 104, 207-215.

[3] Tripathy, N.K., Nabi, M.d.J., Sahu, G.P., and Kumar, A.A., "Genetoxicity testing of two red dyes in the somatic and germ like cells of Drosophila." Food Chem. Toxicol., 1995, 33, 923-927.

[4] Mpountoukas, P., Pantazaki, A., Kostareli, E., Christodoulou, P., Kareli, D., Poliliou, S., Mourelatos, S., Lambropoulou, V. and Lialiaris, T., "Cytogenetic evaluation and DNA interaction studies of the food colorants amaranth, erythrosine and tatrazine." Food Chem. Toxicol., 2010, 48, 2934-2944.

[5] Ritchie, E.E., Princz, J.I., Robidoux, P.Y. and Scroggins, R.P., "Ecotoxicity of xanthene dyes and non-chlorinated bisphenol in soil." Chemosphere., 2013, 90, 2129-2135.

[6] Wang, J., Fan, X. M., Tian, K., Zhou, Z. W. and Wang, Y., "Largely Improved Photocatalytic Properties of Ag/Tetrapod-Like ZnO Nanocompounds Prepared with Different PEG Contents." Appl. Surf. Sci., 2011, 257, 7763-7770.

[7] Hübwer, K., "Bond charge model for the transverse dynamic effective charge and the piezoelectric constant of zinc blende type crystal." Phys. Status Solidi B., 1975, 68, 223-232.

[8] Dou, M. and Persson, C., "Comparative study of rutile and anatase SnO_2 and TiO_2: Band-edge structures, dielectric functions, and polaron effects." J. appl. Phys., 2013, 113, 083703.

[9] Batzill, M. and Diebold, U., "The Surface and Materials Science of Tin Oxide." Prog. Surf. Sci., 2005, 79, 47-154.

[10] Pan, S. S., Shen, Y. D., Teng, X. M., Zhang, Y. X., Li, L., Chu, Z. Q., Zhang, J. P., Li, G. H. and Hu, X., "Substitutional Nitrogen-Doped Tin Oxide Single Crystalline Submicrorod Arrays: Vertical Growth, Band Gap Tuning and Visible Light-Driven Photocatalysis." Mater. Res. Bull., 2009, 44, 2092-2098.

[11] Tang, J. W., Zou, Z. G. and Ye, J. H., "Efficient Photocatalytic Decomposition of Organic Contaminants over $CaBi_2O_4$ under Visible-Light Irradiation." Angew. Chem. Int. Edit., 2004, 43, 4463-4466.

[12] Lee, S. Y. and Park, S. J., "TiO_2 Photocatalyst for Water Treatment Applications." J. Ind. Eng. Chem., 2013, 19, 1761-1769.

[13] Liu, S., Li, C., Yu, J. and Xiang, Q., "Improved visible-light photocatalytic activity of porous carbon self-doped ZnO nanosheet-assembled flowers." Cryst. Eng. Comm., 2011, 13, 2533-2541.

[14] Chiarello, G. L., Aguirre, M. H. and Selli, E., "Hydrogen Production by Photocatalytic Steam Reforming of Methanol on Noble Metal-Modified TiO_2." J. Catal., 2010, 273, 182 – 190.

[15] Yan, J. H., Liu, Q., Guan, L. X., Liang, F. and Gu, H. J., "Photocatalytic Hydrogen Generation of Pt-$Sr(Zr_{1-x}Y_x)O_{3-\delta}$-$TiO_2$ Heterojunction under The Irradiation of Simulated Sunlight." Front. Chem. China., 2009, 4, 121 – 126.

[16] Alem, A. and Sarpoolaki, H., "The Effect of Silver Doping on Photocatalytic Properties of Titania Multilayer Membranes." Solid State Sci., 2010, 12, 1469 – 1472.

[17] Asahi, R., Morikawa, T., Ohwaki, T., Aoki, A. and Taga, Y., "Visible-light Photocatalysis in Nitrogen-Doped Titanium Oxides." Sci., 2001, 293, 269 – 271.

[18] Bu, X. Z., Zhang, G. K., Gao, Y. Y. and Yang, Y. Q., "Preparation and Photocatalytic Properties of Visible Light Responsive N-doped TiO_2/Rectorite composites." Micropor. Mesopor. Mat., 2010, 136, 132 – 137.

[19] Xiao, Q., Ouyang, L.L., Gao, L. and Yao, C., "Preparation and Visible Light Photocatalytic Activity of Mesoporous N, S-Codoped $TiO_2(B)$ Nanobelts." Appl. Surf. Sci., 2011, 257, 3652 – 3656.

[20] Long, M. C., Cai, W. M., Zhou, B. X., Chai, X. Y. and Wu, Y. H., "Efficient Photocatalytic Degradation of Phenol over Co_3O_4/$BiVO_4$ Composite under Visible Light Irradiation." J. phys. Chem., 2006, 110, 20211 – 20216.

[21] Yan, J., Chen, H. and Zhang, L., "Inactivation of Escherichia coli on Immobilized CuO/CoFe$_2$O$_4$-TiO$_2$ Thin-Film under Simulated Sunlight Irradiation." Chin. J. Chem., 2011, 29, 1133 – 1138.

[22] Park, H., Choi, W. and Hoffmann, M. R., "Effects of the Preparation Method of the Ternary CdS/TiO$_2$/Pt Hybrid Photocatalysts on Visible Light-Induced Hydrogen Production." J. Mater. Chem., 2008, 18, 2379-2385.

[23] Paola, A. D., Palmisano, L. and Auguglian, V., "Photocatalytic Behavior of Mixed WO$_3$/WS$_2$ Powders." Catal. Today., 2000, 58, 141-149.

[24] Min, Y. L., Zhang, K., Chen, Y.C. and Zhang, Y.G., "Synthesis of Nanostructured ZnO/Bi$_2$WO$_6$ Heterojunction for Photocatalysis Application." Sep. Purify. Technol., 2012, 92, 115-120.

[25] Arora, S. K., Mathew, T., Chudasama, B. and Kothari, A., "Single Crystal Growth and Photoelectrochemical Study of Copper Tungstate." J. Cryst. Growth., 2005, 275, 651-656.

[26] Pyper, K. J., Yourey, J. E. and Bartlett, B. M., "Reactivity of CuWO$_4$ in Photoelectrochemical Water Oxidation is Dictated by a Midgap Electronic State." J. Phys. Chem. C., 2013, 117, 24726 – 24732.

[27] Despange, F. and Massart, D.L., "Neural Networks in Multivariate Calibration." Analyst., 1998, 123, 157 – 178.

[28] Eswaran, K., Yong R. L., and Kavitha, B., "Fabrication of a visible-light-driven p-type NiWO$_4$/n-type SnO$_2$ heterojunction with efficient photocatalytic activity for degradation of Amaranth." J. Chin. Chem. Soc., 2022, 69, 7, 1020-1031.

[29] Sathishkumar, P., Sweena, R., Wu, J. J. and Anandan, S., "Synthesis of CuO-ZnO Nanophotocatalyst for Visible Light Assisted Degradation of a Textile Dye in Aqueous Solution." Chem. Eng. J., 2011, 171, 136-140.

[30] Nasir, M., Bagwasi, S., Jiao, Y., Chen, F., Tian, B. and Zhang, J., "Characterization and Activity of The Ce and N Co-Doped TiO$_2$ Prepared through Hydrothermal Method." Chem. Eng. J., 2014, 236, 388-397.

[31] Tripathy, S. K. and Yu, Y., "Single Particle Model of SnO$_2$ Deposition on Silver Nanoparticles." Mater. Lett., 2008, 62, 377-380.

[32] Joseph, E. Y. and Bart, M. B., "Electrochemical deposition and photoelectrochemistry of CuWO$_4$, a promising photoanode for water oxidation." J. Mater. Chem., 2011, 21, 7651-7660.

[33] Khyzhun, O.Y., Strunskus, T., Cramm, S. and Solonin, Y. M., "Electronic Structure of CuWO$_4$: XPS, XES and NEXAFS Studies." J. Alloys compd., 2005, 389, 14-20.

[34] Xu, S., Gao, X., Sun, J., Jiang, D., Zhou, F., Liu, W. and Weng, L., "Nanostructured WS$_2$–Ni Composite Films for Improved Oxidation, Resistance and Tribological Performance." Appl. Surf. Sci., 2014, 288, 15–25.

[35] Yen, P. C., Huang, Y. S. and Tiong, K. K., "The Growth and Characterization of Rhenium-Doped WS$_2$ Single Crystals." J. Phys. Condens. Mat., 2004, 16, 2171–2180.

[36] Yang, G., Yan, Z. and Xiao, T., "Preparation and Characterization of SnO$_2$/ZnO/TiO$_2$ Composite Semiconductor with Enhanced Photocatalytic Activity." Appl. Surf. Sci., 2012, 258, 8704-8712.

[37] Kavitha, B., Sharumathi, S. and Sivakumar, S., "Fabrication of MnWO$_4$ modified ZnS nanocomposite as an effective nanoadsorbent: Experimental investigation and neural network modeling." J. Water Environ. Nanotechnol., 2023, 8(1), 79-93.

[38] Kim, J., Lee, J. S. and Kang, M., "Synthesis of Nanoporous Structured SnO$_2$ and its Photocatalytic Ability for Bisphenol A Destruction." Bull. Korean Chem. Soc., 2011, 32, 51715-1720.

[39] Thangavel, S., Venugopal, G. and Kim, S.J., "Enhanced Photocatalytic Efficacy of Organic Dyes using β-Tin Tungstate–Reduced Graphene Oxide Nanocomposites." Mater. Chem. Phy., 2014, 145, 108 -115.

[40] Badr, Y., AbdEl-Wahed, M.G. and Mohamoud, M. A., "Photocatalytic degration of methyl red dye by silica nanoparticles." J. Hazard. Mater., 2008, 154, 245-253.

[41] Fu, Y., Sun, X. and Wang, X., "BiVO$_4$–

graphene Catalyst and Its High Photocatalytic Performance Under Visible Light Irradiation.", Mater. Chem. Phy., 2011, 131, 325 – 330.

[42] Sun, J., Qiao, L., Sun, S. and Wang, G., "Photocalytic degradation of Orange-G on Nitrogen doped TiO_2 catalyst under visible light and sunlight irradiation." J. Hazard. Mater., 2008, 155, 312-319.

[43] Velmurugan, R., and Swaminathan, M., "An Efficient Nanostructured ZnO for Dye Sensitized Degradation of Reactive Red 120 Dye under Solar Light.", Sol. Energy. Mater. Sol. Cells., 2011, 95, 942-950.

13